J. Fluid Mech. (1983), *vol.* 130, *pp.* 123–151
Printed in Great Britain

The breaking of axisymmetric slender liquid bridges

By J. MESEGUER

Laboratorio de Aerodinámica, E.T.S.I. Aeronáuticos, Universidad Politécnica, Madrid, Spain

(Received 20 April 1982 and in revised form 15 September 1982)

Liquids held by surface tension forces can bridge the gap between two solid bodies placed not too far apart from each other. The equilibrium conditions and stability criteria for static, cylindrical liquid bridges are well known. However, the behaviour of an unstable liquid bridge, regarding both its transition toward breaking and the resulting configuration, is a matter for discussion. The dynamical problem of axisymmetric rupture of a long liquid bridge anchored at two equal coaxial disks is treated in this paper through the adoption of one-dimensional theories which are widely used in capillary jet problems.

1. Introduction

Liquid bridges appear in a large variety of industrial processes in which the handling of non-confined liquids is required. A typical example of these processes could be the so-called floating zone melting technique, which has been widely used in recent years in crystal growth and in purification of high-melting-point materials. In this technique, a rod of the material to be purified is placed between two solid supports. The rod is locally heated until the material melts and a small liquid zone is obtained. If the heat source is suitably displaced along the rod, the consecutive sections of the rod melt and solidify progressively and, since the impurities remain in the melt, the solidified rod has a higher purity than the original one, because a great part of the impurities have been carried by the melt to one end of the rod, where they can be disposed of. The advantage of this method is that the melt does not require any crucible since it is held by surface-tension forces. The solidification front can thus be more easily controlled.

However, in the ground laboratory, the maximum stable length of a vertically suspended liquid bridge is controlled by the balance between hydrostatic pressure, which increases with the distance to the top of the molten zone, and surface-tension forces. The use of a reduced-gravity environment partially removes the constraint imposed on the length of the liquid bridge, rendering it more inherently accessible than on Earth.

The maximum length of a liquid bridge, even in zero-gravity conditions, is limited by stability phenomena. The maximum stable length of a cylindrical, circular cross-section liquid bridge at rest was calculated by Rayleigh (1945) when studying the stability of capillary jets: the liquid bridge is stable if its slenderness (that is, the ratio of the length to the undisturbed diameter) is less than π and unstable for slendernesses greater than π.

The study of liquid bridges is a formidable task both because of the material characteristics of the melt, whose properties are strongly temperature-dependent, and because of the complexities associated with the disturbances that could be imposed on the liquid bridge, either accidentally or intentionally. Thus, depending on the aspect of the liquid-bridge problem under study, several simplifications must be introduced in the model. When the aim is to study the mechanical response of the liquid bridge, the simplest approach consists of disregarding phase changes, considering a liquid bridge, with uniform and constant properties, held between two parallel, coaxial solid disks of the same diameter.

Studies on the liquid bridge could be grouped in several categories.

(i) Hydrostatic studies aim to establish the equilibrium shapes and stability of the bridge. These studies involve liquid bridges between equal disks at rest (Haynes 1970; Gillette & Dyson 1971; Martínez 1978*a*), or include the effects of solid-body rotation (Gillis 1961; Martínez 1978*b*, Brown & Scriven 1980). Some aspects of the problem have not yet been treated, such as those related to the stability of liquid bridges with free edges.

A particular application of these studies could consist of detecting molecular forces in liquid films by means of the liquid-bridge configurations (Padday 1976).

(ii) Dynamical studies include the spin-up from rest: the dynamics of the liquid close to the edges when one of the disks starts to rotate (Da Riva & Meseguer 1978) and the movement due to surface-tension gradients induced by a temperature difference between both disks (Napolitano 1978; Schwabe *et al.* 1978; Da Riva & Alvarez 1981) or a non-uniform heating of the interface (Wuest & Chun 1980).

This paper is devoted to the hydrodynamics of cylindrical liquid bridges having slendernesses close to the static stability limit, subjected to axisymmetric disturbances keeping a constant volume. The problem is attacked through one-dimensional models previously used in capillary-jet theory.

2. General equations for the axisymmetric liquid bridge

Let us consider a slender liquid bridge held by surface-tension forces between two parallel, coaxial, equal-diameter solid disks, with anchored edges, as shown in figure 1.

The problem to be solved concerns the evolution of such a liquid bridge under axisymmetric disturbances, so imposed that at the beginning of the process the shape of the interface differs slightly from the cylindrical one.

To carry out this study several assumptions are introduced:

(*a*) internal movement in the liquid bridge is due only to capillary-pressure gradients generated by the deformation of the interface;

(*b*) the gas atmosphere surrounding the liquid does not affect the dynamics of the liquid bridge;

(*c*) gravity as well as inertia forces due to a non-uniform displacement of the liquid bridge as a whole are absent;

(*d*) since only axisymmetric configurations are considered, the problem is independent of the azimuthal coordinate;

(*e*) properties of the liquid (density and viscosity) as well as that of the interface (surface tension) are uniform and constant.

Under such assumptions, the non-dimensional differential equations for the axisymmetric, non-rotating flow in cylindrical coordinates are:

$$\frac{1}{r}\frac{\partial}{\partial r}(rU)+\frac{\partial W}{\partial z}=0, \tag{2.1}$$

$$\frac{\partial U}{\partial t}+U\frac{\partial U}{\partial r}+W\frac{\partial U}{\partial z}=-\frac{\partial P}{\partial r}+C\left(\frac{\partial^2 U}{\partial r^2}+\frac{\partial^2 U}{\partial z^2}+\frac{1}{r}\frac{\partial U}{\partial r}-\frac{U}{r^2}\right), \tag{2.2}$$

$$\frac{\partial W}{\partial t}+U\frac{\partial W}{\partial r}+W\frac{\partial W}{\partial z}=-\frac{\partial P}{\partial z}+C\left(\frac{\partial^2 W}{\partial r^2}+\frac{\partial^2 W}{\partial z^2}+\frac{1}{r}\frac{\partial W}{\partial r}\right), \tag{2.3}$$

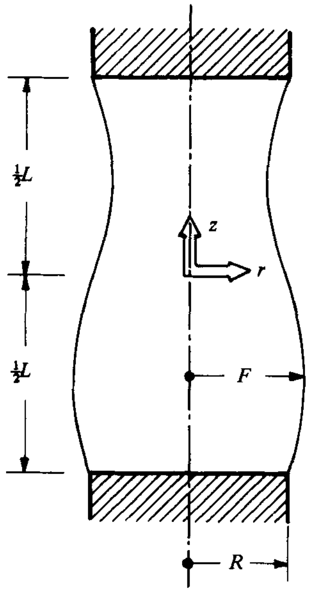

FIGURE 1. Geometry and coordinate system for the perturbed liquid bridge.

where U and W represent the non-dimensional radial and axial velocities respectively. To write down these equations all lengths have been made dimensionless with the radius R of the disks, and all velocities with $(\sigma/\rho R)^{\frac{1}{2}}$, where σ is the surface tension and ρ the liquid density; time has been made dimensionless with $(\rho R^3/\sigma)^{\frac{1}{2}}$, and reduced gauge pressure $(P-P_0)/\rho$ with $\sigma/\rho R$. Finally, C is a non-dimensional parameter giving the ratio of viscous to capillary forces: $C = \nu(\rho/\sigma R)^{\frac{1}{2}}$.

The boundary conditions at the disks are

$$W(r, \pm\Lambda, t) = 0, \tag{2.4}$$

$$U(r, \pm\Lambda, t) = 0, \tag{2.5}$$

where $\Lambda = L/2R$ is the slenderness of the bridge.

At the axis of symmetry

$$U(0, z, t) = 0, \tag{2.6}$$

$$\frac{\partial}{\partial r} W(0, z, t) = 0. \tag{2.7}$$

The first boundary condition at the interface, whose equation is $r = F(z,t)$, will express the balance of normal forces. These forces are the capillary pressure, the excess of the local pressure over the ambient pressure, and the normal viscous stresses. In dimensionless form

$$P - \frac{2C}{1+(\partial F/\partial z)^2}\left[\frac{\partial U}{\partial r} + \left(\frac{\partial F}{\partial z}\right)^2 \frac{\partial W}{\partial z} - \frac{\partial F}{\partial z}\left(\frac{\partial W}{\partial r} + \frac{\partial U}{\partial z}\right)\right]$$
$$= \frac{1}{[1+(\partial F/\partial z)^2]^{\frac{3}{2}}}\left[\frac{1+(\partial F/\partial z)^2}{F} - \frac{\partial^2 F}{\partial z^2}\right]. \tag{2.8}$$

One more boundary condition is deduced by putting the tangential viscous stresses equal to zero at the interface:

$$C\left[2\frac{\partial F}{\partial z}\left(\frac{\partial U}{\partial r}-\frac{\partial W}{\partial z}\right)+\left[1-\left(\frac{\partial F}{\partial z}\right)^2\right]\left(\frac{\partial W}{\partial r}+\frac{\partial U}{\partial z}\right)\right]=0. \tag{2.9}$$

On the other hand, the condition that the interface is a material surface, since the mass-flow rate through it is zero, yields

$$\frac{\partial F}{\partial t}-U+W\frac{\partial F}{\partial z}=0. \tag{2.10}$$

Furthermore, it is assumed that the interface remains anchored to the disk edges:

$$F(\pm A,t)=1. \tag{2.11}$$

The formulation will be completed by fixing suitable initial conditions, i.e.

$$F(z,0)=F_0(z),\quad W(r,z,0)=0,\quad U(r,z,0)=0, \tag{2.12}$$

with

$$\int_{-A}^{A} F_0^2(z)\,\mathrm{d}z=2A$$

(the initial perturbation does not change the cylindrical volume).

An analytical solution of the system of equations (2.1)–(2.3) with conditions (2.4)–(2.12) seems to be unknown even in the linear case, since the attachment condition at the disk edges poses a great problem. If this condition is removed, the problem becomes similar to that of capillary jets, and the well-known Rayleigh solution results directly.

3. One-dimensional slice inviscid model

The complexity of the general formulation may be reduced by using a one-dimensional theory similar to the one used by Lee (1974) in the study of capillary-jet breaking. With this simplification the axial velocity happens to be dependent only upon the axial coordinate and the time, and, considering an inviscid fluid, (2.3) shows that pressure is also constant over each cross-section and dependent only on the axial coordinate and the time. In that case, (2.2) becomes decoupled from the other equations, and it suffices to solve the following equations:

$$\frac{1}{r}\frac{\partial}{\partial r}(rU)+\frac{\partial W}{\partial z}=0, \tag{3.1}$$

$$\frac{\partial W}{\partial t}+W\frac{\partial W}{\partial z}=-\frac{\partial P}{\partial z}. \tag{3.2}$$

With regard to boundary conditions, the axial velocity must be zero at the disks:

$$W(\pm A,t)=0, \tag{3.3}$$

and the interface be anchored at the disk edges:

$$F(\pm A,t)=1. \tag{3.4}$$

Conditions (2.6) and (2.7) are then met automatically.

At the interface, the tangential condition disappears because $C = 0$, whereas the normal condition becomes

$$P = \frac{1}{[1+(\partial F/\partial z)^2]^{\frac{3}{2}}}\left[\frac{1+(\partial F/\partial z)^2}{F} - \frac{\partial^2 F}{\partial z^2}\right]. \tag{3.5}$$

Since the pressure does not depend on r, the above equation relates the pressure jump at any slice to the shape of the interface. The last boundary condition remains:

$$\frac{\partial F}{\partial t} - U + W\frac{\partial F}{\partial z} = 0. \tag{3.6}$$

Finally, initial conditions similar to (2.12) must be added.

To eliminate the velocity U from the previous formulation we may substitute for (3.1) and (3.6) a new equation expressing the overall mass conservation in each cross-section. By application of the continuity principle to a control volume bounded by two contiguous cross-sections and the corresponding interface, the following result is obtained:

$$\frac{\partial F^2}{\partial t} + \frac{\partial}{\partial z}(WF^2) = 0. \tag{3.7}$$

Before pursuing the matter further, it would be pertinent to introduce some considerations on the assumption of the unidimensionality of the problem. This assumption is well justified in capillary jets whenever the ratio of the disturbance wavelength to the undisturbed radius of the jet is large (Pimbley 1976; Pimbley & Lee 1977). In the liquid bridge, a typical wavelength perturbation is determined by the bridge length, and the abovementioned ratio is of the order of twice the slenderness Λ, which is bounded from above by the value $\Lambda = \pi$.

The continuity equation (2.1) allows us to perform an order-of-magnitude analysis of the velocities appearing in the bridge, i.e.

$$\frac{U_c}{R} \sim \frac{W_c}{L}, \tag{3.8}$$

where the subscript c means some characteristic value. On the other hand, since the movement is irrotational ($\nabla \times V = 0$) an additional relationship can be obtained, namely

$$\frac{U_c}{L} \sim \frac{\Delta_r W}{R}, \tag{3.9}$$

Where $\Delta_r W$ stands for the characteristic radial variation of the axial velocity. Thence, the ratio of the convective terms appearing in (2.3) gives

$$\frac{U\dfrac{\partial W}{\partial r}}{W\dfrac{\partial W}{\partial z}} \sim \frac{U_c\dfrac{\Delta_r W}{R}}{W_c\dfrac{W_c}{L}} \sim \left(\frac{R}{L}\right)^2 = \frac{1}{4\Lambda^2} \ll 1, \tag{3.10}$$

that is $\partial W/\partial r \approx 0$ if the slenderness is great enough.

Therefore, for slender liquid bridges the axial velocity can be taken constant over each cross-section, and, from (2.1), the radial velocity varies linearly with the radial coordinate (provided that the minimum radius of the bridge remains of order unity). The same result would be achieved by expanding in Taylor series the Bessel functions that appear in the classical three-dimensional theory of capillary jets, retaining only the first terms.

According to the preceding arguments, the inviscid slice model will fail in the last period of the breaking process (remember that this model does not satisfy the radial momentum equation). However, the results obtained are very encouraging, since they are in fair agreement with the results from more-sophisticated one-dimensional theories (such as the continuum Cosserat model) or from hydrostatic three-dimensional theories.

4. Linear analysis of the inviscid slice model

Let ϵ be a parameter measuring, for instance, the initial deviation of the interface from the cylindrical one; if ϵ is small enough, leaving apart ϵ^2 terms, the variables involved in the problem may be rewritten as

$$F = 1+\epsilon f, \quad P = 1+\epsilon p, \quad W = \epsilon w. \tag{4.1}$$

After substituting these expressions in (3.2), (3.5), (3.7) and conditions (3.3) and (3.4), there results

$$2\frac{\partial f}{\partial t}+\frac{\partial w}{\partial z} = 0, \tag{4.2}$$

$$\frac{\partial w}{\partial t}+\frac{\partial p}{\partial z} = 0, \tag{4.3}$$

$$p = -f-\frac{\partial^2 f}{\partial z^2}, \tag{4.4}$$

$$w(\pm\Lambda, t) = 0, \quad f(\pm\Lambda, t) = 0. \tag{4.5}$$

Introducing in (4.3) the perturbation pressure, as given by (4.4), and eliminating the variable f between (4.2) and (4.3), one obtains

$$2\frac{\partial^2 w}{\partial t^2}+\frac{\partial^2 w}{\partial z^2}+\frac{\partial^4 w}{\partial z^4} = 0, \tag{4.6}$$

which is the differential equation to be satisfied by the axial velocity w, together with boundary conditions

$$w(\pm\Lambda, t) = 0, \quad \left.\frac{\partial w}{\partial z}\right|_{z=\pm\Lambda} = 0, \tag{4.7}$$

where the second condition has been obtained from that expressing the attachment at the disk edges, which states, according to (4.2), that w must vanish with zero slope at the disks.

In a similar way, we could eliminate w from (4.2) and (4.3), yielding the same (4.6) for the shape of the interface, f. However, boundary conditions in this case would be

$$\left.\begin{aligned} f(\pm\Lambda, t) &= 0, \\ \left.\frac{\partial f}{\partial z}\right|_{z=\pm\Lambda}+\left.\frac{\partial^3 f}{\partial z^3}\right|_{z=\pm\Lambda} &= 0, \end{aligned}\right\} \tag{4.8}$$

resulting in a more involved algebra because of the linear combination of derivatives appearing in (4.8).

To solve (4.6) we look for solutions like

$$w = \operatorname{Re}\left(\mathscr{A}\, e^{rt}\mathscr{W}(z)\right), \tag{4.9}$$

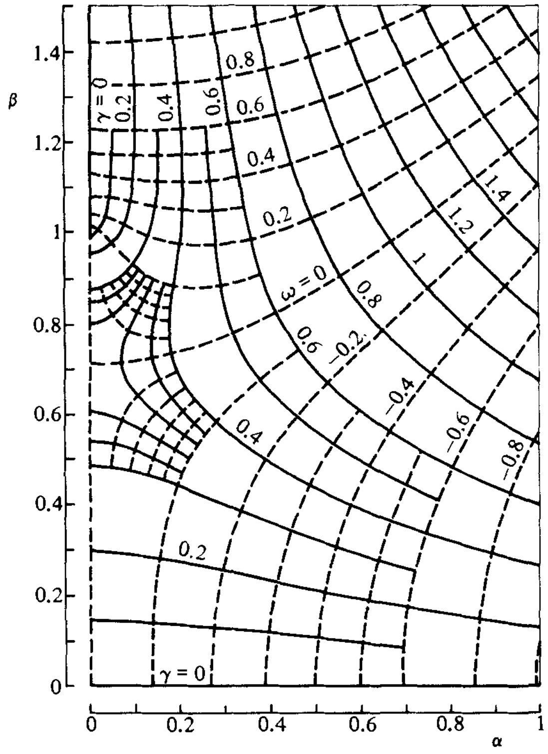

FIGURE 2. Complex plane $\theta(\tau)$, with $\theta = \alpha + \mathrm{i}\beta$ and $\tau = \gamma + \mathrm{i}\omega$, corresponding to solutions of the complex equation $\theta^4 + \theta^2 + 2\tau^2 = 0$. For a given τ the four roots are $\pm\theta_1$ and $\pm\theta_2$, where $\theta_1 = \alpha_1(\gamma, \omega) + \mathrm{i}\beta_1(\gamma, \omega)$, $\theta_2 = \alpha_2(\gamma, -\omega) - \mathrm{i}\beta_2(\gamma, -\omega)$.

where $\mathscr{A}$ and $\tau = \gamma + \mathrm{i}\omega$ are complex numbers, $\mathscr{W}$ is a complex function of the real axial coordinate z, and Re stands for real part. Introduction of (4.9) into (4.6) yields the following ordinary differential equation for $\mathscr{W}$:

$$\frac{\mathrm{d}^4\mathscr{W}}{\mathrm{d}z^4} + \frac{\mathrm{d}^2\mathscr{W}}{\mathrm{d}z^2} + 2\tau^2\mathscr{W} = 0, \tag{4.10}$$

whose solutions are $\mathrm{e}^{\theta z}$, $\theta = \alpha + \mathrm{i}\beta$ being the roots of the characteristic equation

$$\theta^4 + \theta^2 + 2\tau^2 = 0. \tag{4.11}$$

Figure 2 shows a quadrant of the mapping of the roots of (4.11). The complete mapping has two sheets, being symmetrical with respect to the origin. Since this slice model does not include viscosity effects, we are only interested in solutions with a growth factor greater or equal to zero, $\gamma > 0$. Therefore values of γ and ω have been assigned to each curve in the understanding that, for every value of $\tau = \gamma + \mathrm{i}\omega$, the roots of (4.11) are $\pm\theta_1$ and $\pm\theta_2$, with

$$\left.\begin{aligned}\theta_1 &= \alpha_1(\gamma, \omega) + \mathrm{i}\beta_1(\gamma, \omega), \\ \theta_2 &= \alpha_2(\gamma, -\omega) - \mathrm{i}\beta_2(\gamma, -\omega),\end{aligned}\right\} \tag{4.12}$$

where α and β are positive real numbers.

In the general case, the axial velocity will be given by

$$w = \mathrm{Re}\,[\mathrm{e}^{\tau t}(\mathscr{A}\,\mathrm{e}^{\theta_1 z} + \mathscr{B}\,\mathrm{e}^{-\theta_1 z} + \mathscr{C}\,\mathrm{e}^{\theta_2 z} + \mathscr{D}\,\mathrm{e}^{-\theta_2 z})], \tag{4.13}$$

where $\mathscr{A}$, $\mathscr{B}$, $\mathscr{C}$ and $\mathscr{D}$ are complex constants. After some calculations we obtain

$$\begin{aligned} w = {} & \mathrm{e}^{\gamma t}\cos\omega t\,[\mathrm{e}^{\alpha_1 z}(A_1\cos\beta_1 z - A_2\sin\beta_1 z) + \mathrm{e}^{-\alpha_1 z}(B_1\cos\beta_1 z + B_2\sin\beta_1 z) \\ & + \mathrm{e}^{\alpha_2 z}(C_1\cos\beta_2 z - C_2\sin\beta_2 z) + \mathrm{e}^{-\alpha_2 z}(D_1\cos\beta_2 z + D_2\sin\beta_2 z)] \\ & - \mathrm{e}^{\gamma t}\sin\omega t\,[\mathrm{e}^{\alpha_1 z}(A_1\sin\beta_1 z + A_2\cos\beta_1 z) + \mathrm{e}^{-\alpha_1 z}(-B_1\sin\beta_1 z + B_2\cos\beta_1 z) \\ & + \mathrm{e}^{\alpha_2 z}(C_1\sin\beta_2 z + C_2\cos\beta_2 z) + \mathrm{e}^{-\alpha_2 z}(-D_1\sin\beta_2 z + D_2\cos\beta_2 z)]. \end{aligned} \qquad (4.14)$$

Boundary conditions (4.7) state that w and its derivative must be zero at the disks at any time. To meet these conditions we must consider that the two major terms contributing to w must satisfy each boundary condition separately. Thence an homogeneous system of algebraic equations is obtained, with the eight unknowns A_1, A_2, B_1, …, D_2, whose determinant must be zero in order to provide non-trivial solutions:[†]

$$D(\gamma,\omega,\Lambda) \equiv \begin{vmatrix} d_{11} & d_{12} & \cdots & d_{18} \\ d_{21} & d_{22} & \cdots & d_{28} \\ \vdots & \vdots & & \vdots \\ d_{81} & d_{82} & \cdots & d_{88} \end{vmatrix} = 0. \qquad (4.15)$$

The problem is now to find out the values of Λ, γ and ω (that is, the roots $\theta_i = \alpha_i + \mathrm{i}\beta_i$) for which (4.15) is zero. Obviously, these eigenvalues should be found numerically, because of the order of the determinant $D(\gamma, \omega, \Lambda)$.

It can be seen that no eigenvalues are found if both γ and ω have simultaneously a non-zero value. Therefore the only possibilities are $\gamma = 0$, $\omega \neq 0$ (oscillation) or $\gamma \neq 0$, $\omega = 0$ (breaking), as one can expect from a linear inviscid model. In such cases the complexity of the solution is drastically reduced because of the nature of the roots in (4.11), and it is possible to rearrange (4.14) to yield simpler expressions for w which only depend on four unknown constants.

4.1. *Oscillation*

When $\gamma = 0$, $\omega \neq 0$, figure 2 shows that the roots of (4.11) are of the form $\pm\alpha$, $\pm\mathrm{i}\beta$, with $\alpha^2 - \beta^2 = 1$, $\alpha\beta = \surd 2\,\omega$. Thence the axial velocity and the shape of the interface are given by

$$w = \sin\omega t(A\,\mathrm{e}^{\alpha z} + B\,\mathrm{e}^{-\alpha z} + C\cos\beta z + D\sin\beta z), \qquad (4.16)$$

$$f = \frac{1}{2\omega}\cos\omega t\,[\alpha(A\,\mathrm{e}^{\alpha z} - B\,\mathrm{e}^{-\alpha z}) + \beta(-C\sin\beta z + D\cos\beta z)]. \qquad (4.17)$$

From the application of boundary conditions (4.7) to (4.16) the following eigenvalue equation results:

$$\cosh\alpha\Lambda\sinh\alpha\Lambda\cos\beta\Lambda\sin\beta\Lambda - \surd 2\,\omega\,(\cosh^2\alpha\Lambda\sin^2\beta\Lambda - \sinh^2\alpha\Lambda\cos^2\beta\Lambda) = 0, \qquad (4.18)$$

whose solutions are plotted in figure 3(*a*), giving the pulsation ω versus the slenderness Λ of the liquid bridge.[‡]

[†] The eight equations are obtained by applying the boundary conditions to (4.14), resulting in four equations for the first term of (4.14) and another four equations for the second one. These equations are omitted here because of their complexity. Additional details can be obtained upon request from the author.

[‡] In Figure 3 and the following figures, where results are plotted as functions of the slenderness Λ, the first non-trivial eigenvalue, as obtained from the corresponding eigenvalue equation is the only one plotted. The second and following eigenvalues appear for slendernesses out of the range in which we are interested.

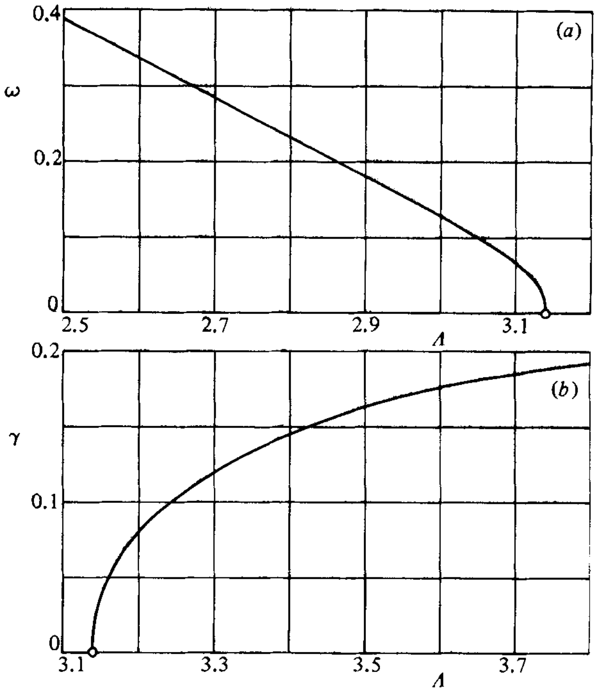

FIGURE 3. Pulsation ω and growth factor γ versus the slenderness A. Results obtained from the linear analysis of the one-dimensional slice model.

Three of the constants appearing in (4.16) and (4.17) may be expressed as functions of the fourth. By eliminating one of the four equations resulting from the fulfilment of the boundary conditions, and solving the resulting system:

$$B = A\frac{K_{b\omega}}{K_{a\omega}}, \quad c = A\frac{K_{c\omega}}{K_{a\omega}}, \quad D = A\frac{K_{d\omega}}{K_{a\omega}}, \tag{4.19}$$

where

$$\left.\begin{aligned} K_{a\omega} &= -\beta\,\mathrm{e}^{\alpha A} + \mathrm{e}^{-\alpha A}(\beta\cos 2\beta A + \alpha\sin 2\beta A), \\ K_{b\omega} &= \beta\,\mathrm{e}^{-\alpha A} - \mathrm{e}^{\alpha A}\,(\beta\cos 2\beta A - \alpha\sin 2\beta A), \\ K_{c\omega} &= 4\cosh\alpha A\,(\beta\cos\beta A\sinh\alpha A - \alpha\sin\beta A\cosh\alpha A), \\ K_{d\omega} &= 4\sinh\alpha A\,(\alpha\cos\beta A\sinh\alpha A + \beta\sin\beta A\cosh\alpha A). \end{aligned}\right\} \tag{4.20}$$

The constant A may be determined from initial conditions. If according to (4.1) we impose the condition that ϵ be the only parameter measuring the initial disturbance of the interface, we must choose $A = 2\omega/|g_{\min}|$, where $g_{\min}$ stands for the minimum value of the spatial term in (4.17), after introducing (4.20).

4.2. *Breaking*

In the case $\gamma \neq 0$, $\omega = 0$ several possibilities are present, depending on the values of γ, as figure 2 shows. If $\gamma < \frac{1}{4}\sqrt{2}$ the roots of (4.11) are imaginary, and if $\gamma > \frac{1}{4}\sqrt{2}$ the roots are complex of the general form (4.12); $\gamma = \frac{1}{4}\sqrt{2}$ implies the double roots $\pm \mathrm{i}\frac{1}{2}\sqrt{2}$.

Calculations show that for $\gamma \geqslant \frac{1}{4}\sqrt{2}$ the only attainable solution is $A = 0$, therefore we restrict our analysis to the case $\gamma < \frac{1}{4}\sqrt{2}$. When this inequality holds, the roots

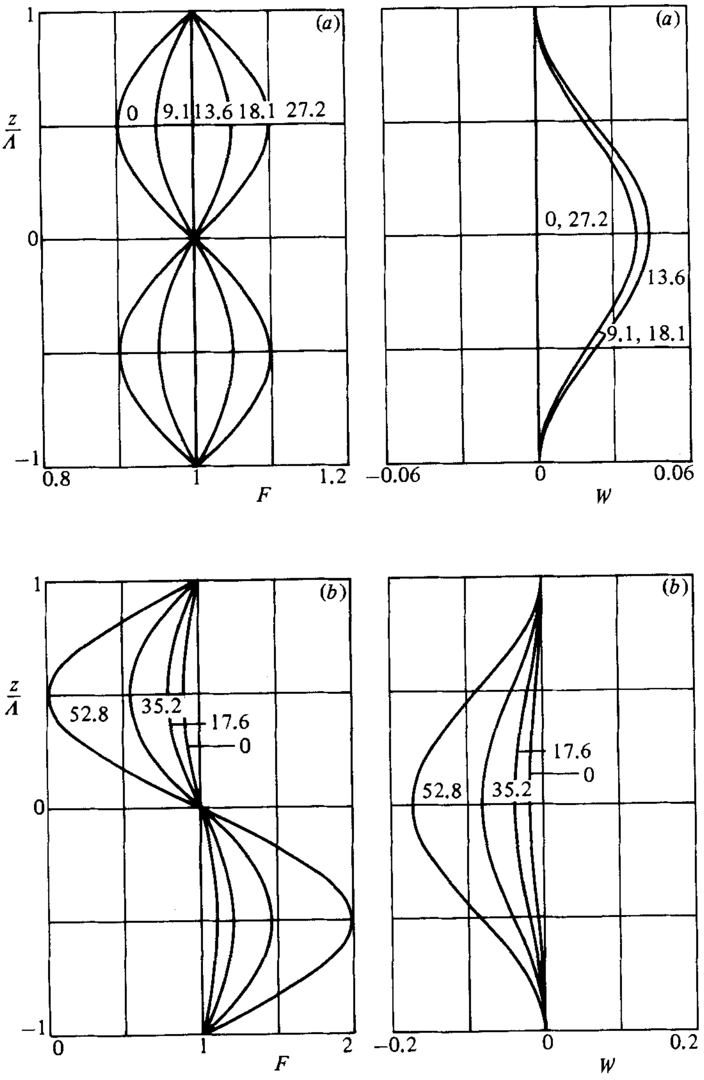

Figure 4. Variation with time of the shape of the liquid bridge $F = 1+\epsilon f$ and the axial velocity field $W = \epsilon w$ for slender liquid bridges having $\epsilon = 0.1$ and $\Lambda = 3.03$ (*a*) and 3.16 (*b*) respectively. Numbers on the curves indicate the elapsed non-dimensional time from the initial time. Results obtained from the one-dimensional slice linearized model.

of (4.11) are $\pm i\beta_1$, $\pm i\beta_2$, with $\beta_1^2+\beta_2^2 = 1$, $\beta_1\beta_2 = \sqrt{2}\,\gamma$, and the expressions for the velocity w and the shape f are

$$w = e^{\gamma t}(A\cos\beta_1 z + B\sin\beta_1 z + C\cos\beta_2 z + D\sin\beta_2 z), \tag{4.21}$$

$$f = -\frac{1}{2\gamma}e^{\gamma t}[\beta_1(-A\sin\beta_1 z + B\cos\beta_1 z) + \beta_2(-C\sin\beta_2 z + D\cos\beta_2 z)]. \tag{4.22}$$

Now the eigenvalue equation is

$$\sin 2\beta_1\Lambda\sin 2\beta_2\Lambda - 2\sqrt{2}\,\gamma\,(1-\cos 2\beta_1\Lambda\cos 2\beta_2\Lambda) = 0, \tag{4.23}$$

whose roots, the growth factor γ versus the slenderness Λ, are plotted in figure 3(*b*).

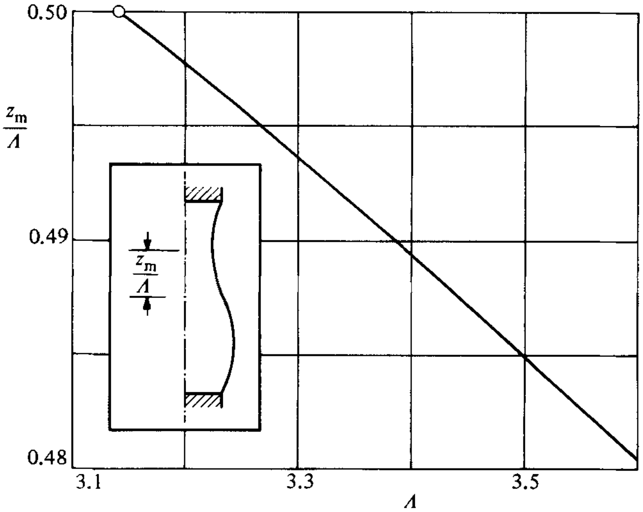

FIGURE 5. Position of the neck of the liquid bridge z_m/Λ versus the slenderness Λ. Results obtained from the linear analysis of the one-dimensional slice model.

We may express again three of the integration constants in terms of the fourth. By repeating the same process as before, there results

$$B = -AK_\gamma \frac{\sin \beta_2 \Lambda}{\cos \beta_2 \Lambda}, \quad C = -A\frac{\cos \beta_1 \Lambda}{\cos \beta_2 \Lambda}, \quad D = AK_\gamma \frac{\sin \beta_1 \Lambda}{\cos \beta_2 \Lambda}, \tag{4.24}$$

with K_γ given by

$$K_\gamma = \frac{\beta_1 \sin \beta_1 \Lambda \cos \beta_2 \Lambda - \beta_2 \cos \beta_1 \Lambda \sin \beta_2 \Lambda}{\beta_2 \sin \beta_1 \Lambda \cos \beta_2 \Lambda - \beta_1 \cos \beta_1 \Lambda \sin \beta_2 \Lambda}. \tag{4.25}$$

With the same criterion for ϵ as stated in the preceding case, we can fix $A = -2\gamma/|g_{\min}|$.

It should be noted that, as figure 3 indicates, this dynamic linearized model furnishes the abovementioned stability limit for cylindrical liquid zones. If the slenderness is less than π, a small perturbation causes oscillation of the zone, with a frequency $\omega/2\pi$. In the other hand, if $\Lambda > \pi$, disturbances grow exponentially with time, and the zone breaks up. Figure 4 shows the variation with time of both the velocity profile and the interface shape as obtained from this linearized model for bridges whose slendernesses are respectively smaller and bigger than the stability limit.

Another important feature shown by this linear analysis is that, according to (4.22), the position of the neck bridge depends on its slenderness (figure 5). This indicates that the volume of each of the two caps resulting from the bridge breakdown depends on Λ, the volume of the main drop being smaller as Λ increases.

5. Cosserat one-dimensional model

Within the Cosserat approximation the liquid bridge is modelled as a one-dimensional continuum: a curve (the symmetry axis) at each point of which there are two deformable vectors, other than the tangent vector, which are kinematically independent of the displacement and its derivatives. Such deformable vectors are called 'directors'.

Developments of this theory are mainly related to solid rods in elasticity (Green & Laws 1966; Green, Naghdi & Wenner 1974*a*, *b*). For fluid 'rods' the general model yields a system of infinite equations with infinite unknowns which requires further simplifying hypothesis to reach analytically treatable equations.

In this paper we use the one-dimensional axisymmetric-jet equations for a viscous incompressible fluid given by Green (1976) and Bogy (1978). These equations are conveniently adapted to the particularities of the liquid bridge. It should be pointed out that this Cosserat formulation leads to a velocity field similar to that of the inviscid slice model: axial velocity is independent of r, whereas the radial velocity varies linearly with r:

$$V(r,z,t) = W(z,t)\,\boldsymbol{e}_z + rU^*(z,t)\,\boldsymbol{e}_r, \tag{5.1}$$

where $\boldsymbol{e}_z$ and $\boldsymbol{e}_r$ are unit vectors in the axial and radial directions respectively.

This theory will introduce some of the main features of the three-dimensional problem defined in §2, and represents an improvement on the inviscid slice model in that it accounts for transverse inertia and (partially) viscous effects.

The complete set of one-dimensional Cosserat equations is, in non-dimensional form:

$$\frac{\partial F^2}{\partial t} + \frac{\partial}{\partial z}(F^2 W) = 0, \tag{5.2}$$

$$\begin{aligned}\tfrac{1}{8}F^4\left[\frac{\partial^2 W}{\partial z\,\partial t} + W\frac{\partial^2 W}{\partial z^2} - \frac{1}{2}\left(\frac{\partial W}{\partial z}\right)^2\right]\\ = -P + \frac{F}{K}\left(1 - \frac{F}{K^2}\frac{\partial^2 F}{\partial z^2}\right) + \tfrac{1}{8}F^2 C\left(4F\frac{\partial F}{\partial z}\frac{\partial^2 W}{\partial z^2} + F^2\frac{\partial^3 W}{\partial z^3} - 8\frac{\partial W}{\partial z}\right),\end{aligned} \tag{5.3}$$

$$F^2\left(\frac{\partial W}{\partial t} + W\frac{\partial W}{\partial z}\right) = -\frac{\partial P}{\partial z} + \frac{2}{K}\frac{\partial F}{\partial z}\left(1 - \frac{F}{K^2}\frac{\partial^2 F}{\partial z^2}\right) + 2FC\left(2\frac{\partial F}{\partial z}\frac{\partial W}{\partial z} + F\frac{\partial^2 W}{\partial z^2}\right), \tag{5.4}$$

where

$$K = \left[1 + \left(\frac{\partial F}{\partial z}\right)^2\right]^{\frac{1}{2}}.$$

Equation (5.2) is the continuity equation, while (5.3) and (5.4) come from momentum balance in the radial and axial directions, and incorporate incompressiblity in the elimination of the director velocity U^*, which is related to the axial velocity through $U^* = -\frac{1}{2}\partial W/\partial z$, as in the inviscid slice model.

Equations (5.2)–(5.4) must be completed with suitable boundary conditions at the end disks,

$$W(\pm A, t) = 0, \quad F(\pm A, t) = 1, \tag{5.5}$$

and initial conditions

$$W(z,0) = W_0(z), \quad F(Z,0) = F_0(z). \tag{5.6}$$

Equations (5.3) and (5.4) can be reduced to one single equation by differentiation of (5.3) with respect to z and subtraction of (5.4). This yields

$$\begin{aligned}\frac{\partial W}{\partial t} + W\frac{\partial W}{\partial z} - \tfrac{1}{2}F\frac{\partial F}{\partial z}\left[\frac{\partial^2 W}{\partial z\,\partial t} + W\frac{\partial^2 W}{\partial z^2} - \frac{1}{2}\left(\frac{\partial W}{\partial z}\right)^2\right] - \tfrac{1}{8}F^2\left(\frac{\partial^3 W}{\partial z^2\,\partial t} + W\frac{\partial^3 W}{\partial z^3}\right)\\ = \frac{1}{K}\frac{\partial F}{\partial z}\left[\frac{1}{F^2} + \frac{1}{FK^2}\frac{\partial^2 F}{\partial z^2} - \frac{3}{K^4}\left(\frac{\partial^2 F}{\partial z^2}\right)^2\right] + \frac{1}{K^3}\frac{\partial^3 F}{\partial z^3}\\ + C\left[\frac{6}{F}\frac{\partial F}{\partial z}\frac{\partial W}{\partial z} + \left[3 - \frac{3}{2}\left(\frac{\partial F}{\partial z}\right)^2 - \frac{F}{2}\frac{\partial^2 F}{\partial z^2}\right]\frac{\partial^2 W}{\partial z^2} - F\frac{\partial F}{\partial z}\frac{\partial^3 W}{\partial z^3} - \frac{F^2}{8}\frac{\partial^4 W}{\partial z^4}\right],\end{aligned} \tag{5.7}$$

which, together with (5.2) and conditions (5.5) and (5.6), constitute the general Cosserat model for the liquid bridge.

6. The inviscid Cosserat linearized model

In a similar way as in §4, let ϵ be a parameter small enough to allow the expansion of the variables in the form

$$F = 1+\epsilon f, \quad W = \epsilon w, \tag{6.1}$$

leaving apart higher-order terms.

By introducing (6.1) in (5.2), (5.7), (5.5) and (5.6), the following linearized set of equations and boundary conditions is obtained:

$$2\frac{\partial f}{\partial t}+\frac{\partial w}{\partial z} = 0. \tag{6.2}$$

$$\frac{\partial w}{\partial t}-\frac{1}{8}\frac{\partial^3 w}{\partial z^2\,\partial t} = \frac{\partial f}{\partial z}+\frac{\partial^3 f}{\partial z^3}+C\left(3\frac{\partial^2 w}{\partial z^2}-\frac{1}{8}\frac{\partial^4 w}{\partial z^4}\right). \tag{6.3}$$

$$w(\pm\Lambda, t) = 0, \quad f(\pm\Lambda, t) = 0, \tag{6.4}$$

$$w(z,0) = w_0(z), \quad f(z,0) = f_0(z). \tag{6.5}$$

From now on the process to be followed is similar to that of §4: elimination of f between (6.2) and (6.3) yields

$$\frac{\partial^2 w}{\partial t^2}-\frac{1}{8}\frac{\partial^4 w}{\partial z^2\,\partial t^2}+\frac{1}{2}\frac{\partial^2 w}{\partial z^2}+\frac{1}{2}\frac{\partial^4 w}{\partial z^4}-3C\frac{\partial^3 w}{\partial z^2\,\partial t}+\frac{C}{8}\frac{\partial^5 w}{\partial z^4\,\partial t} = 0, \tag{6.6}$$

with the boundary conditions

$$w(\pm\Lambda, t) = 0, \quad \left.\frac{\partial w}{\partial z}\right|_{z=\pm\Lambda} = 0. \tag{6.7}$$

Since we are interested in solutions like (4.9), introducing that expression into (6.6), the following ordinary differential equation for the complex function $\mathcal{W}$ results:

$$(1+\tfrac{1}{4}C\tau)\frac{\mathrm{d}^4\mathcal{W}}{\mathrm{d}z^4}+(1-\tfrac{1}{4}\tau^2-6C\tau)\frac{\mathrm{d}^2\mathcal{W}}{\mathrm{d}z^2}+2\tau^2\mathcal{W} = 0, \tag{6.8}$$

whose solutions $\mathrm{e}^{\theta z}$ must satisfy the characteristic equation

$$(1+\tfrac{1}{4}C\tau)\,\theta^4+(1-\tfrac{1}{4}\tau^2-6C\tau)\,\theta^2+2\tau^2 = 0. \tag{6.9}$$

In the inviscid case, $C = 0$ (6.9) reduces to

$$\theta^4+(1-\tfrac{1}{4}\tau^2)\,\theta^2+2\tau^2 = 0, \tag{6.10}$$

which is analogous to (4.11) except for the term $-\frac{1}{4}\tau^2$. Plotting the roots of (6.10) yields a mapping quite similar to that of figure 2.

Thence, in the inviscid case, Cosserat and slice models are similar in the range of values of γ and ω of interest. For example, in the breaking case, $\omega = 0$, the value of γ separating imaginary roots from complex ones is $\gamma = 0.3431$ for the Cosserat model instead of $\gamma = \frac{1}{4}\sqrt{2} = 0.3536$ obtained from the slice model. Because of this similarity all developments made in §§4.1 and 4.2 are valid here. When $\gamma = 0$, $\omega \neq 0$ (oscillation) the velocity field is given by (4.16) and the shape of the interface by (4.17); when $\gamma \neq 0$, $\omega = 0$ (breaking) the expressions to be used are (4.21) and (4.22)

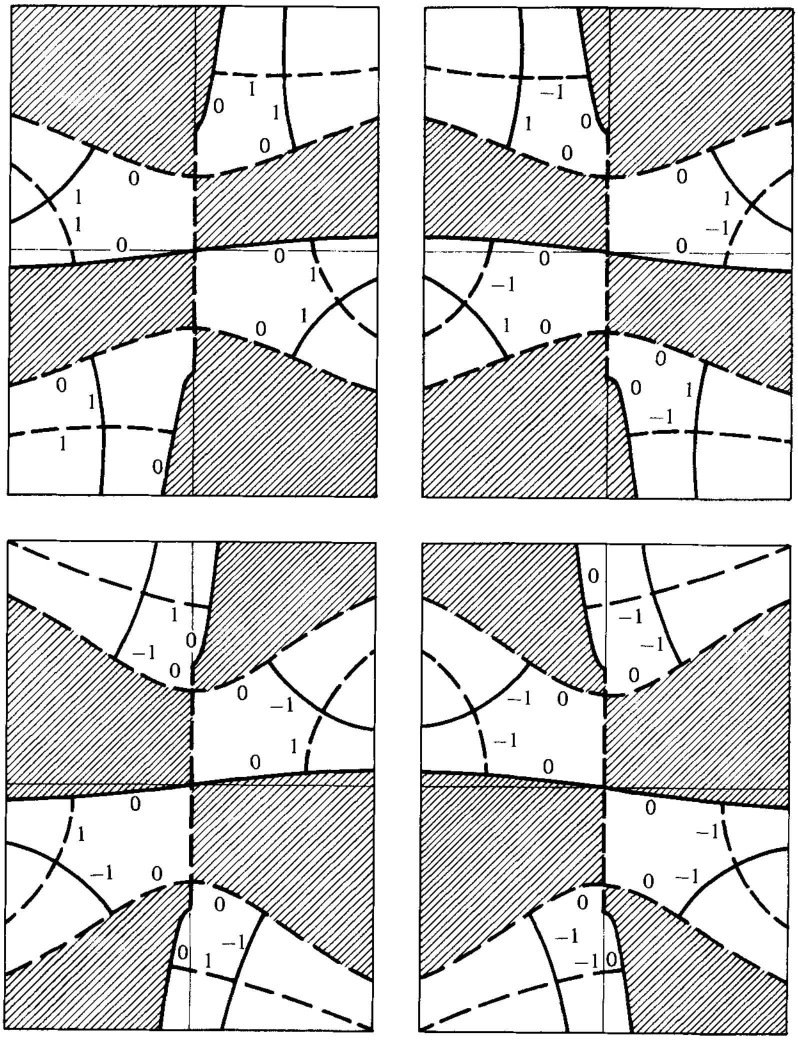

FIGURE 6. Sketch of the plane of the roots of the complex equation (6.9) for a value of the parameter of viscosity $C = 0.1$. The mapping has been split into four maps according to the sign of the real and imaginary parts of $\tau = \gamma + i\omega$. In each map, the shadow areas denote forbidden zones from the assigned signs of γ and ω. ——, γ = constant; – – –, ω = constant.

respectively. Eigenvalue equations, expressions for the integration constants, etc. are the same, with the only difference that now the roots are calculated through (6.10) instead of (4.11).

7. Influence of the viscosity on the dynamics of the liquid bridge

When viscosity is taken into account, the problem is rather different; viscosity distorts the roots map, though it continues to have two sheets, being symmetrical with respect to the origin, but with the two sheets not coinciding. For each point of the mapping there are two couples of curves γ = constant and ω = constant.

The several possibilities are sketched in figure 6, which shows the roots of (6.9) for

$C = 0.1$.† The plane has been split into four maps according to the signs of γ and ω. After this mapping, it suffices to fix the point (γ, ω) on it to obtain directly the four roots of (6.9); conversely, once a root $\theta = \alpha + \mathrm{i}\beta$ is found, the mapping gives the values of γ and ω from which that root can be reached.

To study the influence of the viscosity it will be convenient to take into account our previous experience with the solution of the inviscid cases, and introducing some simple, but helpful, physical ideas in our reasoning.

We can expect that beyond the stability limit, $\Lambda > \pi$, the viscosity will not change the character of the solutions; thence the bridge will break for these values of the slenderness. This means $\gamma > 0, \omega = 0$ and imaginary roots in (6.9), which is in complete agreement with figure 6 since it is possible to reach this kind of root from $\omega = 0$.

Furthermore, when $C \neq 0$, pure oscillatory solutions must be forbidden, as figure 6 shows. Notice that this solution type corresponds to $\gamma = 0$, and, according to what happened in the inviscid case, the roots of (6.9) should be $\pm\alpha$, $\pm\mathrm{i}\beta$. This is no longer possible, since the curves $\gamma = 0$ do not coincide with the coordinate axis in figure 6. Thence for $\Lambda < \pi$ solutions must either decay with time ($\gamma < 0$, $\omega = 0$) or be oscillatory damped solutions ($\gamma < 0$, $\omega \neq 0$), which agrees with the experimental evidence.

7.1. *Oscillation*

As we stated above, it is not possible to find roots of the form $\pm\alpha$, $\pm\mathrm{i}\beta$, when $\gamma = 0$, $\omega \neq 0$, except when $C = 0$. However, provided that the model reproduces with some approximation the behaviour of a real liquid bridge, there must exist some values of γ, ω and Λ, when $C \neq 0$, for which the determinant (4.15) vanishes, no matter what the nature is of the roots of (6.9).

The mentioned values have been obtained numerically by an iterative process: fixing Λ, from a suitable initial point (γ, ω) one moves over the surface $\boldsymbol{D} = \boldsymbol{D}(\gamma, \omega)$ in the direction of the steepest slope until reaching the bottom of the appropriate sharp hole corresponding to $\boldsymbol{D} = 0$ (some care is needed in the choice of the departure point (γ, ω) as there is another hole $\boldsymbol{D} = 0$ at the origin for every value of Λ). Figure 7 shows the results of the calculations; in figure 7(*a*) the values of ω versus Λ are plotted for several values of C, the same occurs in figure 7(*b*) with γ instead of ω. As can be seen from these plots, the value of Λ corresponding to $\omega = 0$ decreases as C increases. Thence, if Λ is far enough from π, the bridge, when slightly perturbed, oscillates with damping amplitude. Viscosity causes the frequency to be smaller and decreases damping time.

7.2. *Breaking*

In this case, owing to the nature of the roots of (6.9), all the expressions developed in §4.2 are valid here. Figure 8 shows the results obtained by solving the eigenvalue equation (4.23) for several values of C.

Curves have been plotted as continuous thick lines till the respective vertical tangent points, and as dashed lines from these points onwards, since this part of the curves has no physical meaning (these values give damped evolutions even for $\Lambda > \pi$).

---

† Before pursuing the matter further, it is convenient to give an idea of the practical values of C. If one considers common liquids, such as water and silicone oils, which are used for liquid-bridge experimentation, densities are close to 10^3 kg m^{-3}, viscosities range from, let us say, 10^{-6} m^2 s^{-1} to 10^{-4} m^2 s^{-1}, and surface tensions from 7×10^{-2} N m^{-1} to 2×10^{-2} N m^{-1}; thence, from the definition of $C = \nu(\rho/\sigma R)^{\frac{1}{2}}$, and considering liquid bridges held between disks having 10^{-2} m radius, C varies from 10^{-3} to 10^{-1}, the smaller value corresponding to water.

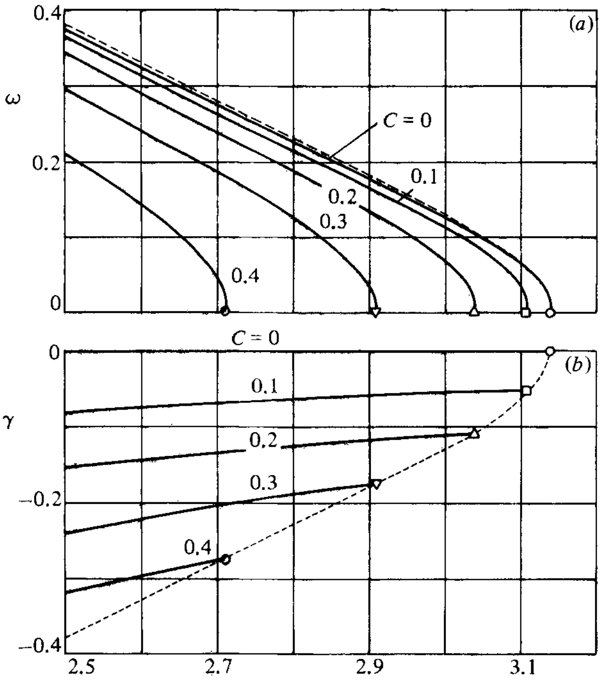

FIGURE 7. Pulsation ω and growth factor γ versus the slenderness Λ. The number on the curves indicate the value of the parameter of viscosity C. Results obtained from the linear analysis of the Cosserat one-dimensional model for the liquid bridge. The thin dashed line plotted in (*a*) corresponds to the results obtained from the one-dimensional slice linearized model.

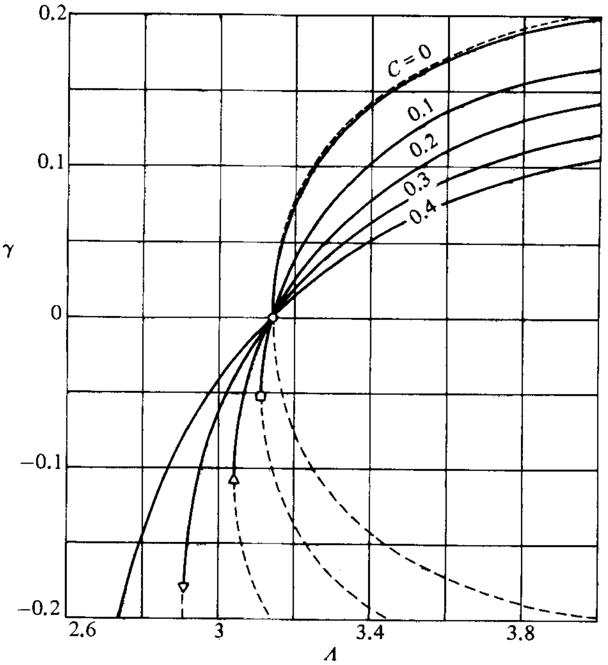

FIGURE 8. Growth factor γ versus the slenderness Λ. The numbers on the curves indicate the value of the parameter of viscosity C. Results obtained from the linear analysis of the Cosserat one-dimensional model for the liquid bridge. The thin dashed line plotted in the top represents the results obtained from the one-dimensional slice linearized model.

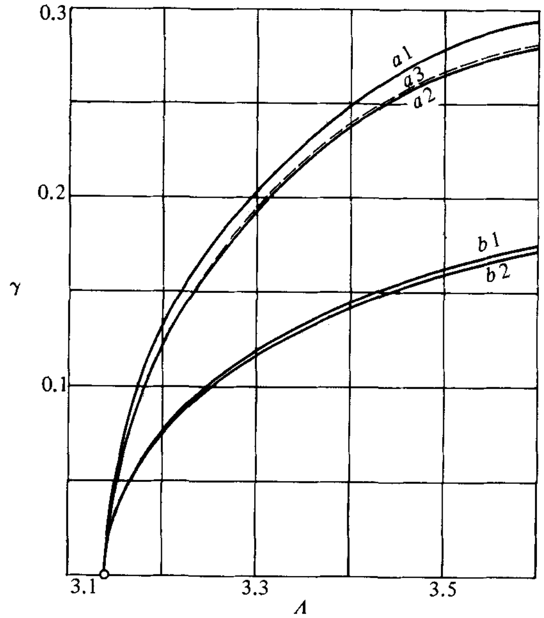

FIGURE 9. Growth factor γ versus Λ. In this plot Λ represents both the slenderness of the zone or the wavelength of the perturbation in the case of capillary jets. The curves represent the results obtained from several linearized models: *a*1, Lee's one-dimensional model for jets; *a*2, Cosserat one-dimensional model for jets; *a*3, Rayleigh three-dimensional model for jets; *b*1, one-dimensional slice model for the liquid bridge; *b*2, Cosserat one-dimensional model for the liquid bridge.

As figure 8 shows, all the curves pass through the point $(\pi, 0)$, thence the effect of viscosity does not change the stability limit. Moreover, for $\Lambda > \pi$ the growth factor decreases as C increases: the breakdown time increases with viscosity, as one would expect.

Another feature shown in figure 8 is that it is possible to obtain pure damping solutions ($\gamma < 0$), depending upon the value of C, for slendernesses slightly less than the stability limit, $\Lambda = \pi$.

8. Liquid bridges versus capillary jets

Since the two linearized analyses §§4, 6 and 7) have been performed by using theories borrowed from capillary jets, it seems appropriate to finish these linearized studies by comparing the results here obtained with those for the jets. Thus, figure 9 shows the growth factor γ for an inviscid, homogeneous and incompressible jet versus the wavelength of the imposed perturbation, also represented by Λ in this plot, as obtained through three different linearized theories. With $k = \pi/\Lambda$, these results are as follows:

(*a*) *One-dimensional Lee model*

$$\gamma^2 = \tfrac{1}{2}k^2(1-k^2); \tag{8.1}$$

(*b*) *One-dimensional Cosserat model*

$$\gamma^2 = \frac{4k^2(1-k^2)}{8+k^2}; \tag{8.2}$$

(c) *Three-dimensional Rayleigh model*

$$\gamma^2 = k(1-k^2)\frac{I_1(k)}{I_0(k)}, \tag{8.3}$$

where I_0 and I_1 are the hyperbolic Bessel functions of zeroth and first order respectively. Figure 9 also includes the previous results obtained for the liquid bridge when $C = 0$.

Several points should be emphasized. First, the one-dimensional results for jets are very good if one compares them with those from three-dimensional theory. Secondly, the behaviour of the liquid bridge is quite different from that of jets: breakdown times are much larger in liquid bridges.

The difference may be explained because of the disks, which force the bridge to remain attached to the edges and cause the velocity to be zero, with zero slope, in sections where the jet velocity reaches its maximum value (that is, in the sections where the radius remains constant with the time).

9. Nonlinear numerical analysis

The general equations of the one-dimensional inviscid slice model for the liquid bridge, (3.2), (3.5) and (3.7), have been integrated numerically by a finite-difference method† assuming that the bridge, initially at rest, is axisymmetrically perturbed.

The variables chosen for the calculations are the same as in Lee (1974), i.e. $S = F^2$, which represents the cross-sectional area of the zone, and $Q = F^2W$, which is proportional to the axial momentum of a slice. By using these variables the abovementioned equations become

$$\frac{\partial S}{\partial t} + \frac{\partial Q}{\partial z} = 0, \tag{9.1}$$

$$\frac{\partial Q}{\partial t} + \frac{\partial}{\partial z}\left(\frac{Q^2}{S}\right) = -S\frac{\partial P}{\partial z}, \tag{9.2}$$

where the pressure is related to S through

$$P = \frac{2}{[4S+(\partial S/\partial z)^2]^{\frac{1}{2}}}\left[1-\frac{2S\,\partial^2 S/\partial z^2-(\partial S/\partial z)^2}{4S+(\partial S/\partial z)^2}\right]. \tag{9.3}$$

Boundary conditions are

$$Q(\pm A, t) = 0, \quad S(\pm A, t) = 1, \tag{9.4}$$

and the imposed initial conditions are

$$S(z,0) = 1+\epsilon(\epsilon-2)\sin\frac{\pi z}{A}, \quad Q(z,0) = 0. \tag{9.5}$$

The initial shape of the zone is assumed to be sinusoidal in the cross-sectional area S and not in the radius F, since with this choice the volume of the distorted zone exactly equals that of the cylindrical shape; moreover, the initial shape is quite similar to those obtained by neutral-buoyancy technique (Plateau tank simulation) when the densities of both liquids, zone and surrounding bath, are not exactly equal (small axial gravity equilibrium shapes).

---

† Calculations were performed by means of the Lax–Wendroff method for finite-difference equations on a Hewlett-Packard 9845B desktop computer using HP-BASIC language.

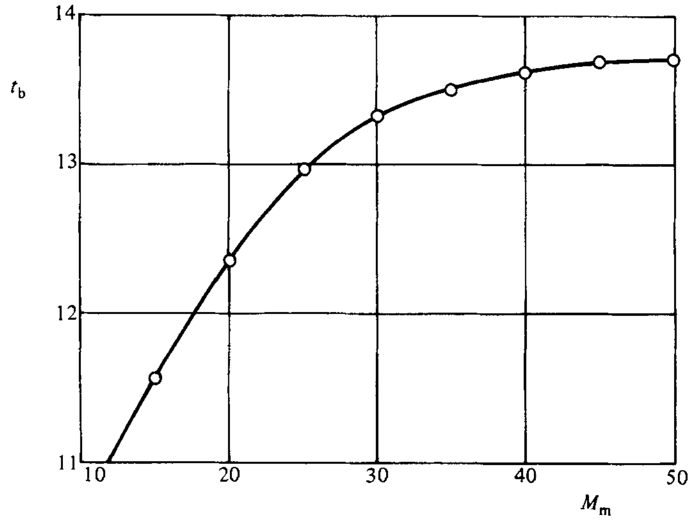

FIGURE 10. Non-dimensional breaking time t_b versus the number of points M_m of the spatial grid. The results correspond to a liquid bridge having $\Lambda = 3.14$ and $\epsilon = 0.2$.

9.1. *Some comments on numerical computations*

The above equations are hyperbolic differential equations for which numerical methods have been extensively studied.

The Lax–Wendroff method (Roache 1972; Mitchell & Griffiths 1980) consists in developing in Taylor series with respect to time, retaining terms up to order $(\Delta t)^2$:

$$\left.\begin{aligned} S(z,t+\Delta t) &= S(z,t)+\Delta t\frac{\partial}{\partial t}S(z,t)+\frac{(\Delta t)^2}{2}\frac{\partial^2}{\partial t^2}S(z,t)+\dots,\\ Q(z,t+\Delta t) &= Q(z,t)+\Delta t\frac{\partial}{\partial t}Q(z,t)+\frac{(\Delta t)^2}{2}\frac{\partial^2}{\partial t^2}Q(z,t)+\dots,\end{aligned}\right\} \tag{9.6}$$

and the time derivatives appearing in (9.6) are calculated through (9.1)–(9.3) in terms of the spatial derivatives.†

A typical feature of problems where surface-tension effects are present is the high order of the spatial derivatives involved. In our particular case these derivatives have been calculated through a five-point difference scheme. Since the approximation in numerical evaluation of derivatives decreases as the order of differentiation increases, erroneous results will be obtained when the accuracy is not good enough. In this case, however, the accuracy can be controlled through the size Δz, of the spatial grid.

Another source of error could be associated with the five-point scheme used to calculate the derivatives when these derivatives are evaluated close to the boundary points. This scheme introduces four outer points (two external points at each disk) in which the values of S and Q must be calculated to meet boundary conditions (see appendix). Since these outer values are used to calculate the variables at the new time

---

† The continuity equation (9.1) and the momentum equation (9.2) give the first two time derivatives directly in terms of the spatial ones, once $\partial P/\partial z$ is calculated through (9.3). Differentiation of (9.1) with respect to time and of (9.2) with respect to z allows us to eliminate $\partial^2 Q/\partial z\,\partial t$ between these two equations, obtaining $\partial^2 S/\partial t^2$ as a function of the spatial derivatives only. In a similar fashion, time differentiation of (9.2), taking into account the expressions already calculated, gives $\partial^2 Q/\partial t^2$. Additional details can be obtained upon request from the author.

$\epsilon = 0.1$			$\epsilon = 0.2$			$\epsilon = 0.3$			$\epsilon = 0.4$		
Λ	t_b	V_p	Λ	t_b	V_p	Λ	t_b	V_p	Λ	t_b	V_p
3.20	20.5	0.8430	3.20	11.5	0.8441	3.20	7.0	0.8447	3.20	4.2	0.8506
3.16	25.0	0.8465	3.14	13.7	0.8494	3.10	8.4	0.8539	3.10	4.8	0.8565
3.13	33.5	0.8495	3.09	17.7	0.8534	3.01	11.7	0.8607	3.00	5.6	0.8622
			3.07	22.0	0.8553	2.98	15.6	0.8630	2.89	8.5	0.8693
Λ	$\frac{1}{4}T$					2.97	19.6	0.8636	2.85	17.7	0.8716
3.11	81.0		Λ	$\frac{1}{4}T$							
3.09	29.2		3.05	39.7		Λ	$\frac{1}{4}T$		Λ	$\frac{1}{4}T$	
3.03	15.3		3.02	20.0		2.95	20.9		2.83	15.7	
2.92	9.5		2.93	11.4		2.89	12.2		2.82	14.1	
2.80	6.9		2.80	7.3		2.80	8.8		2.80	12.0	

ϵ, initial deformation as in (9.5); Λ, slenderness of the liquid bridge; t_b, breaking time; V_p breaking volume (see figure 11); T, oscillation period

TABLE 1

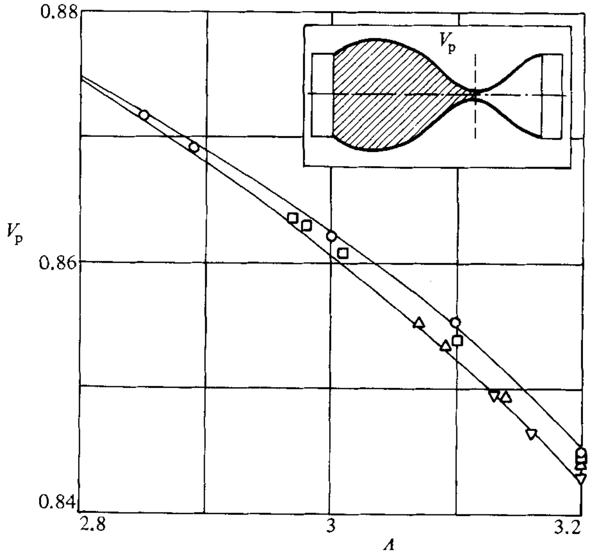

FIGURE 11. Non-dimensional volume V_p versus the slenderness Λ. V_p has been defined as that fraction of the initial volume remaining between one of the disks and the neck section just at the breaking time. The symbols indicate the value of the initial disturbance ϵ: ▽, 0.1; △, 0.2; □, 0.3; ○, 0.4.

level at the disks and the next inner points, the outer points introduce some spurious information in calculations, whose effect decreases as Δz.

The first computations were performed aiming at establishing the optimum of this grid size, running a testing case ($\Lambda = 3.14$, $\epsilon = 0.2$) several times and varying each time the number of steps M_m between the disks ($\Delta z = \Lambda / M_m$). The results obtained are plotted in figure 10, which shows that the breaking time, t_b increases with M_m, but the rate of increase tends to zero for large M_m (the slope is practically zero at $M_m = 50$). For calculations we used $M_m = 40$, which gives, according to figure 10, a breakup time higher than 99 % of that obtained from $M_m = 50$.

Equations (9.1)–(9.3) (see the preceding footnote) enable computation of the state variables S and Q at $t + \Delta t$ in terms of their respective values at t. However, a successful computation depends on the ability to control the numerical stability. In particu-

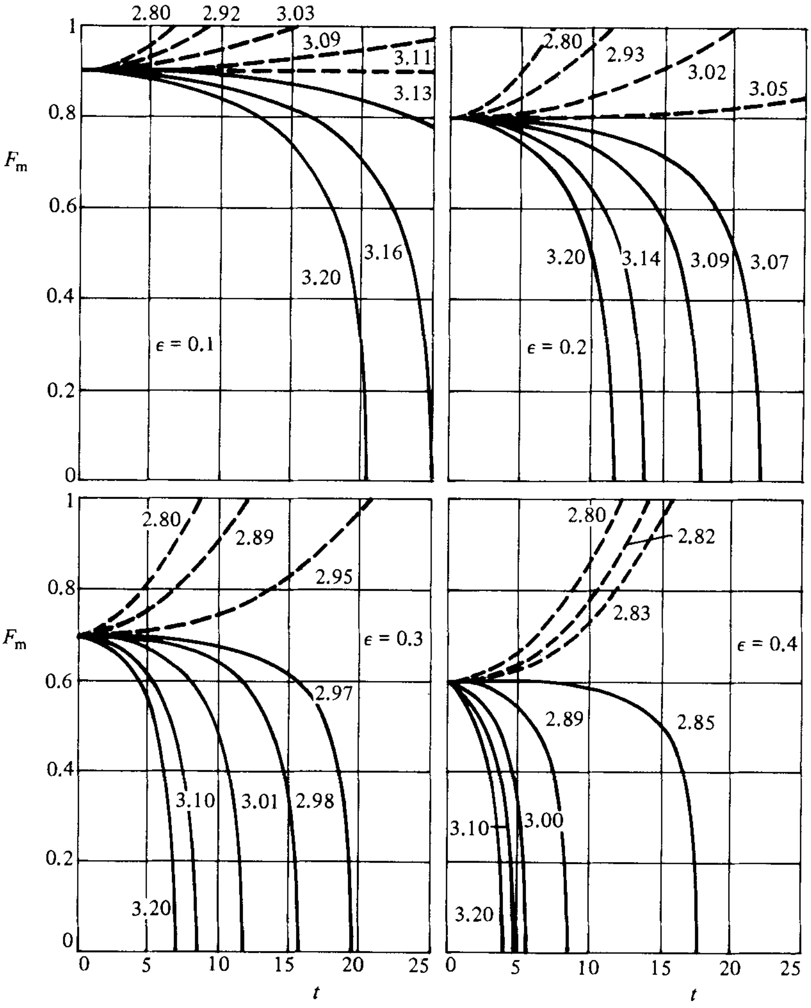

FIGURE 12. Neck radius F_m of the liquid bridge versus non-dimensional time t for several values of the initial deformation ϵ. The numbers on the curves indicate the value of the slenderness Λ. Results obtained by solving numerically the general one-dimensional slice model.

lar, since Δz is already fixed, the grid size of Δt is such that the predicted states must be within the boundaries of characteristics. Owing to nonlinear characteristics, this range varies with time. Thus a variation of the time step Δt is required. One scheme used here consists in limiting the maximum increment of the variables S and Q at each step in such a way that these increments remain nearly constants over all calculations. So Δt is reduced, if the size is not acceptable, until these limitations are fulfilled.

9.2. *Numerical results*

The program has been run for several values of the slenderness Λ and the initial disturbance ϵ, as table 1 shows. In all the cases where breaking takes place, the breaking point occurs at a distance from one of the disks between 65 and 68 % of the corresponding length of the bridge. In such cases the zone breaks up into two caps (leaving apart satellite droplets) whose volumes depend on the slenderness rather than on the initial disturbance, as figure 11 shows.

The complete results are summarized in figure 12, where the variation of the value

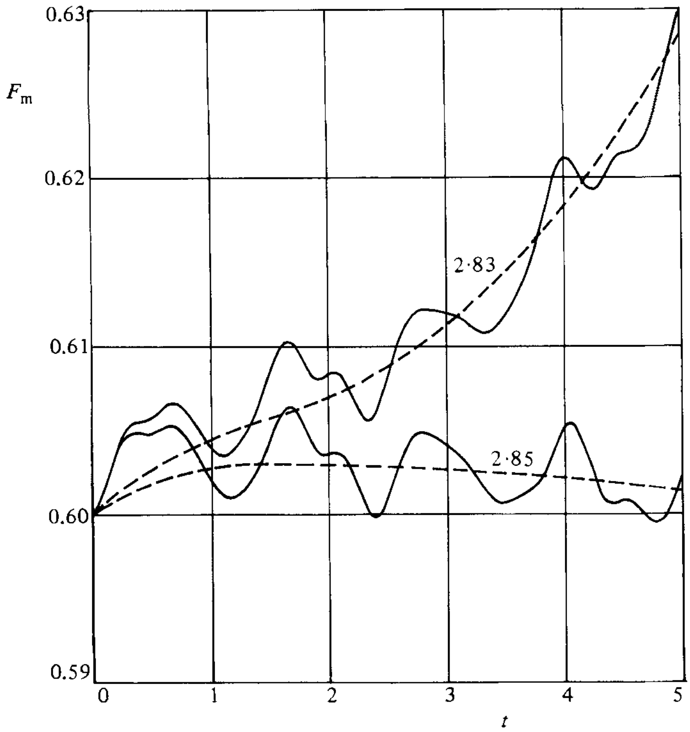

FIGURE 13. Neck radius F_m versus non-dimensional time t. Results correspond to zones having $\epsilon = 0.4$ and $\Lambda = 2.85$ and $\Lambda = 2.83$ respectively. The oscillations around the dashed lines show the short-period rearrangement superimposed on the main evolution.

of the neck radius F_m versus the time t has been plotted. Breakup time t_b is reached when the neck radius vanishes, and the oscillation period T turns out to be equal to four times the time spent by the neck radius in reaching unity.

An important feature shown by computations, which does not appear in figure 12 owing to the scale used, is that the evolution of the zone exhibits two superimposed behaviours: a main one (breaking or oscillation) superimposed on another of small period and amplitude (rearrangement). To understand this rearrangement we must take into account the fact that initially the shape of the zone is not an equilibrium one and the initial pressure field is not evenly distributed. Thence, at the beginning, the zone reacts by generating a velocity field tending to smooth out the pressure distribution, slightly changing the shape of the zone. Thus, since the liquid is assumed to be inviscid, the neck radius oscillates around some mean value, which, in turn, is determined at each moment by the main evolution. The rearrangement becomes more important as ϵ increases. Figure 13 shows this secondary oscillation. It can be seen that the short-period motion is the same in both cases, which supports the above reasoning.

Coming back to the main motion, figure 14 has been plotted from the data of table 1, giving the breakup time and the oscillation period as functions of Λ and ϵ. Obviously, for each value of ϵ the two curves cannot cross each other, since the zone either breaks up or oscillates. Thus each pair of curves defines a value of Λ for which the evolution time is infinitely large (that for unstable equilibrium).

Figure 15 shows the (Λ, ϵ) mapping with the curves t_b = constant, T = constant,

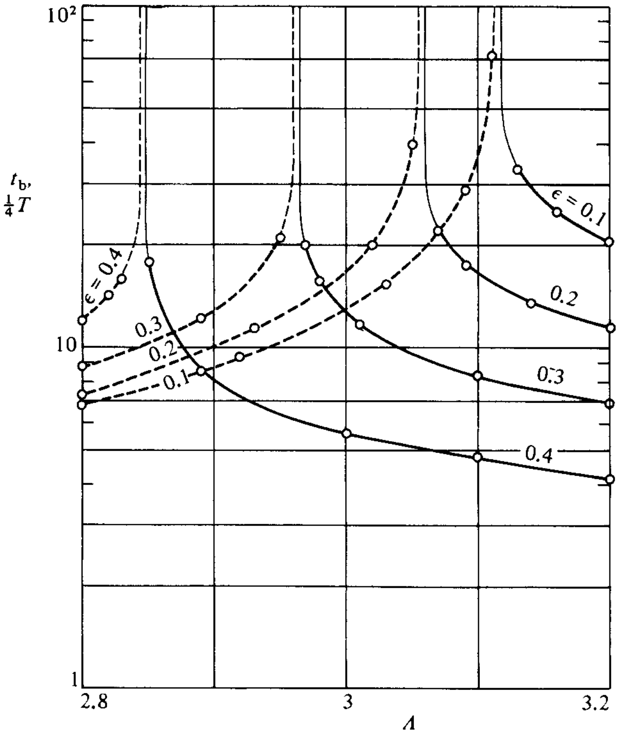

FIGURE 14. Non-dimensional breaking time t_b or oscillation period T versus the slenderness Λ for several values of the initial deformation ϵ. In this plot one-quarter of the oscillation period (dashed lines) has been plotted instead of the whole period because of scale constraints.

which have been derived from figure 14. One can see clearly the border between the breaking and the oscillation region. This limiting curve, corresponding to unstable equilibrium shapes, was calculated by Martínez (1978*a*) in studying the branching from symmetrical to non-symmetrical shapes which appears for $\Lambda = \pi$ in the hydrostatic analysis of the liquid bridge. This curve has also been plotted in figure 15.

As figure 15 shows, the slice model gives excellent results. For high values of ϵ this nonlinear analysis predicts breakup for slendernesses slightly smaller that those obtained from hydrostatic studies, although the difference is always less than 1 % for the considered range of values of Λ and ϵ.

The stability of the liquid bridge under symmetrical disturbances has been also checked. As is known, the stability limit for this type of perturbation is close to $\Lambda = 4.5$ (Martínez 1978*a*). Figure 16 shows the evolution with time of the neck radius of liquid bridges whose initial shape is given by

$$S(z,0) = 1+\frac{\epsilon(2-\epsilon)}{1-\cos\delta}\left(\cos\delta-\cos\frac{\delta z}{\Lambda}\right), \qquad (9.7)$$

where $\delta = 0.4934$ rad. This perturbation is symmetrical with respect to the middle plane of the bridge, it satisfies the boundary conditions, and, for each pair of values Λ and ϵ, its volume is equal to that of the undisturbed cylindrical bridge having the same slenderness.

As figure 16 shows, the liquid bridge oscillates under this kind of symmetrical

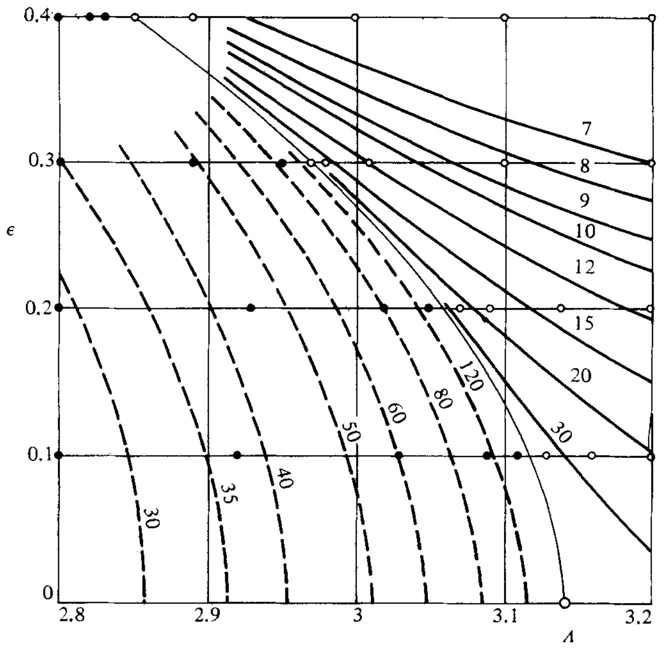

FIGURE 15. Variation with slenderness Λ and initial disturbance ϵ of the non-dimensional breaking time (continuous lines) and the oscillation period (dashed lines). The small circles represent numerical results, indicating the behaviour of the zone: ●, oscillation; ○, breaking. The thin continuous line separating the oscillation region from the breaking one corresponds to unstable equilibrium shapes calculated by Martínez (1978*a*).

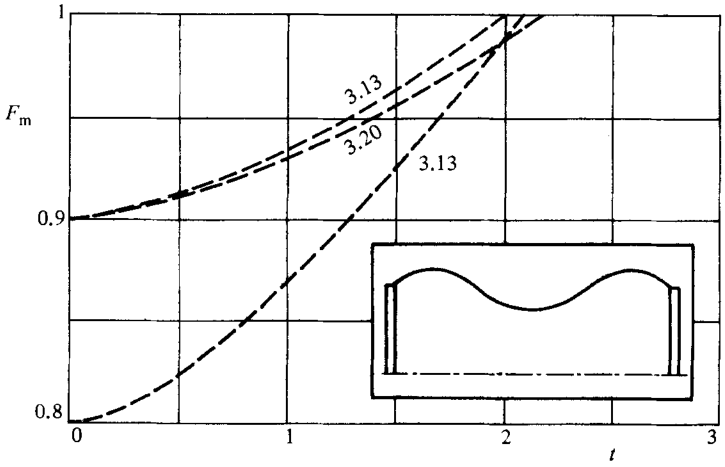

FIGURE 16. Neck radius F_m versus non-dimensional time t for symmetrically perturbed liquid bridges (as sketched in the insert). Numbers on the curves indicate the value of the slenderness Λ. The two upper curves correspond to $\epsilon = 0.1$ and the lower to $\epsilon = 0.2$.

perturbations, even for values of Λ and ϵ for which the bridge would break under non-symmetric perturbations, and the oscillation period becomes greater as Λ increases.

These cases, however, are not of great interest, as any real perturbation will be split into its symmetrical and non-symmetrical components, and the non-symmetrical

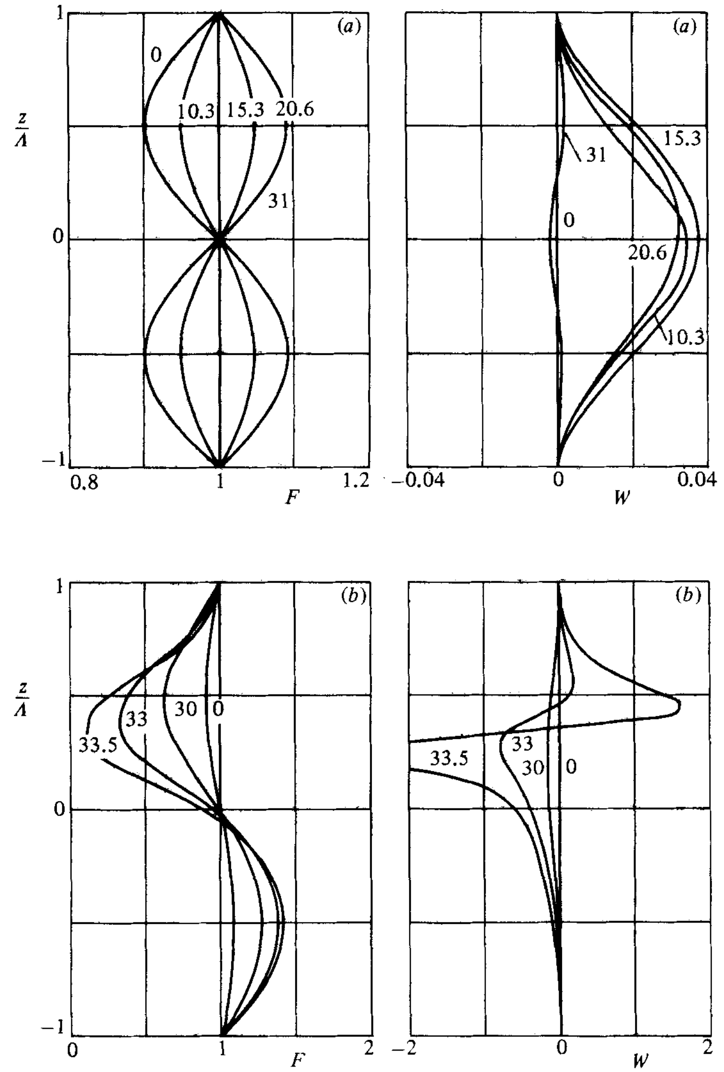

Figure 17. Variation with time of the shape F of the liquid bridge and the axial velocity field W for slender liquid bridges having $\epsilon = 0.1$ and $\Lambda = 3.03$ (*a*) and 3.13 (*b*) respectively. Numbers on the curves indicate the elapsed non-dimensional time from the initial time. Results obtained by numerically solving the general one-dimensional slice model.

component will force the breaking of the zone if the initial conditions belong to the unstable region plotted in figure 15.

To conclude this analysis, figure 17 shows the variation with time of the shape of the bridge and the axial velocity field for two bridges with $\epsilon = 0.1$, having $\Lambda = 3.03$ and 3.13 respectively (as one can see, these results are very different, especially in the breakup case, to those obtained from the linear analysis, which are plotted in figure 4). Figure 18 shows the path followed by tracers placed on the free surface in a meridional plane parallel to the plane of the figure, as calculated from this nonlinear analysis. The paths corresponding to tracers placed inside the liquid bridge can be easily obtained, because in the slice model, in each cross-section, the axial velocity does not depend on r, and the radial velocity, which is calculated from the axial one

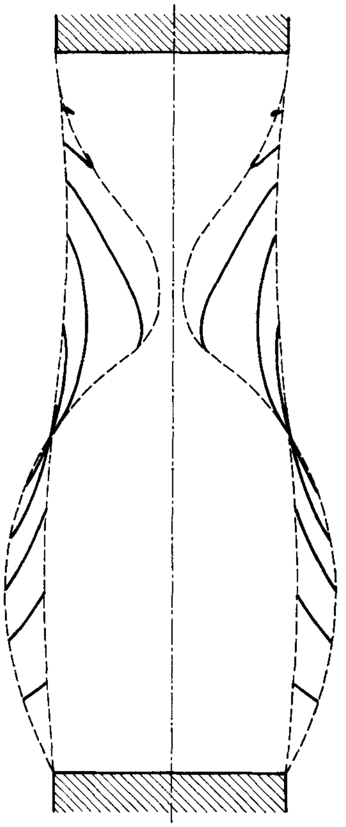

FIGURE 18. Breaking of a slender floating zone having $\Lambda = 3.13$ and $\epsilon = 0.1$. The continuous lines indicate the paths followed by tracers placed at the interface.

through the continuity equation (3.1), varies linearly with this coordinate. However, the observed paths for these internal tracers will differ from the real paths because of the curved interface of the bridge, which distorts the real pattern. Calculation of the real paths followed by internal tracers from the observed paths constitutes a problem not yet solved, which causes problems in checking theoretical and experimental results.

10. Conclusions

The work presented above gives the main features of the breaking of slender, inviscid, axisymmetric liquid bridges in zero gravity.

Although the one-dimensional assumption limits the range of slenderness to which the theory can be applied, the results obtained agree in this range with those from hydrostatic theory and offer a guide about the response of the liquid bridge under axisymmetric disturbances. However, the work is not complete, and additional effort is needed on several aspects not included in this paper, such as the influence of viscosity through a nonlinear analysis, and the dynamics of short liquid bridges to which one-dimensional simplifications are not applicable. It is our impression that the first effect could be dealt with, without excessive extra work, by numerical integration of the Cosserat model once the inviscid problem has been solved.

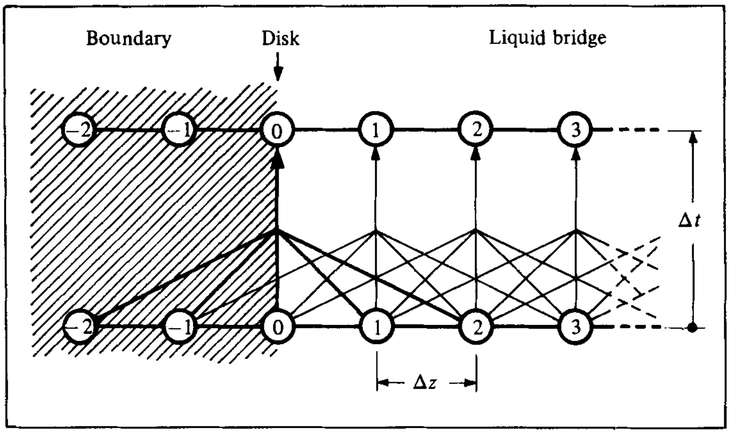

FIGURE 19. Sketch of the numerical integration in a boundary point using a five-point scheme for the evaluation of the spatial derivatives.

This work has been supported by the Spanish National Committee for Space Research (CONIE) under a contract with the Polytechnic University of Madrid (UPM), and is part of a more general endeavour for predicting the behaviour of a liquid bridge subjected to mechanical disturbances in a reduced-gravity environment (ESA experiment 1-ES-331, 1st Spacelab Mission).

I wish to thank Prof. I. Da Riva and Dr I. Martínez for helpful discussions.

Appendix. Numerical boundary conditions

The boundary conditions (zone attached to the disks, with vanishing velocity at these points) must be translated into appropriate numerical boundary conditions. According to (9.6), provided that S and Q have the correct values at time t, the boundary conditions require that these values do not change with time, i.e. all derivatives with respect to time of S and Q must be zero at the disks. In terms of the spatial derivatives, these conditions can be expressed as:

$$\frac{\partial S}{\partial t} = 0 \rightarrow \frac{\partial Q}{\partial z} = 0, \tag{A 1}$$

$$\frac{\partial^2 S}{\partial t^2} = 0 \rightarrow \frac{\partial Q}{\partial z} = \frac{\partial P}{\partial z} = \frac{\partial^2 P}{\partial z^2} = 0, \tag{A 2}$$

$$\frac{\partial Q}{\partial t} = 0 \rightarrow \frac{\partial P}{\partial z} = 0, \tag{A 3}$$

$$\frac{\partial^2 Q}{\partial t^2} = 0 \rightarrow \frac{\partial P}{\partial z} = \frac{\partial^2 P}{\partial z\, \partial t} = \frac{\partial Q}{\partial z} = 0, \tag{A 4}$$

all the derivatives being evaluated at $z = \pm \Lambda$. As we use five-point space centred differences (because of the high order of the spatial derivatives involved) we need to introduce two outer points at each disk, where the values of S and Q at each time step are needed in order to evaluate the derivatives at the disks (see figure 19). The values of S and Q at the outer points are calculated in such a way that boundary conditions are met. This can be accomplished in two stages as follows.

Let S_M and Q_M denote the values of S and Q at the point M, and let us denote by an asterisk the same values when unknown. At time t all the values are known, including those at the outer points. From this level t we can reach the values of S and Q at level $t \pm \Delta t$, except in the outer points, where the centred space algorithm has no application.

Referring to one of the bounds (obviously the process is the same at the other bound), conditions (A 1)–(A 4) show that the last two expressions in (A 2) depend only upon S, so that we can solve first the nonlinear algebraical system corresponding to the two expressions. For the left disk

$$\begin{aligned} P_z(S^*_{-2}, S^*_{-1}, S_0, S_1, S_2) &= 0, \\ P_{zz}(S^*_{-2}, S^*_{-1}, S_0, S_1, S_2) &= 0, \end{aligned} \qquad \text{(A 5)}$$

where the only unknowns are S^*_{-1} and S^*_{-2}. Once S is known in all the points of the grid at time $t+\Delta t$ we evaluate Q^*_{-1} and Q^*_{-2}. The two conditions yet to be satisfied are $\partial Q/\partial z = 0$ and $\partial^2 P/\partial z\, \partial t = 0$, which give the following nonlinear system:

$$\begin{aligned} Q_z(Q^*_{-2}, Q^*_{-1}, Q_0, Q_1, Q_2) &= 0, \\ P_{zt}(Q^*_{-2}, Q^*_{-1}, Q_0, Q_1, Q_2, S_{-2}, S_{-1}, S_0, S_1, S_2) &= 0. \end{aligned} \qquad \text{(A 6)}$$

By solving this system, all S_M and Q_M are known at $t+\Delta t$ and a new iteration begins.

REFERENCES

Bogy, D. B. 1978 Use of one-dimensional Cosserat theory to study instability in a viscous liquid jet. *Phys. Fluids* **21**, 190–197.

Brown, R. A. & Scriven, L. E. 1980 The shape and stability of captive rotating drops. *Phil. Trans. R. Soc. Lond.* **A297**, 51–79.

Da Riva, I. & Alvarez, E. 1981 A regular perturbation approach to surface tension driven flows. *IAF*-81-128, *XXXII IAF Congress, Roma.*

Da Riva, I. & Meseguer, J. 1978 On the structure of the floating zone in melting. *Acta Astronautica* **5**, 637–653.

Gillette, R. D. & Dyson, D. C. 1971 Stability of fluid interface of revolution between equal solid circular plates. *Chem. Engng J.* **2**, 44–45.

Gillis, J. 1961 Stability of a column of rotating viscous liquid. *Proc. Camb. Phil. Soc.* **57**, 152–159.

Green, A. E. 1976 On the nonlineal behaviour of fluid jets. *Int. J. Engng Sci.* **14**, 49–63.

Green, A. E. & Laws, N. 1966 A general theory of rods. *Proc. R. Soc. Lond.* **A293,** 145–155.

Green, A. E., Naghdi, P. M. & Wenner, M. L. 1974*a* On the theory of rods, I. Derivations from the three-dimensional equations. *Proc. R. Soc. Lond.* **A337**, 451–483.

Green, A. E., Naghdi, P. M. & Wenner, M. L. 1974*b* On the theory of rods. II. Developments by direct approach. *Proc. R. Soc. Lond.* **A337**, 485–507.

Haynes, J. M. 1970 Stability of a fluid cylinder. *J. Colloid Interface Sci.* **32**, 652–654.

Lee, H. C. 1974 Drop formation in a liquid jet. *IBM J. Res. Dev.* **18**, 364–369.

Martínez, I. 1978*a* Hidrostática de la zona flotante. Tesis doctoral, Universidad Politécnica de Madrid.

Martínez, I. 1978*b* Floating zone – equilibrium shapes and stability criteria. In *Cospar: Space Research*, vol. XVIII (ed. M. J. Rycroft & A. C. Strickland), pp. 519–522. Pergamon.

Mitchell, A. R. & Griffiths, D. F. 1980 *The finite difference method in partial differential equations.* Wiley.

Napolitano, L. G. 1978 Microgravitational fluid dynamics. In *Proc. 2nd Levich Cong. Washington.*

PADDY, J. F. 1976 Capillary forces and stability in zero-gravity environments. In *Material Sciences in Space, ESA* SP 114. Paris: ESA.

PIMBLEY, W. T. 1976 Drop formation from a liquid jet: a linear one-dimensional analysis considered as a boundary value problem. *IBM J. Res. Dev.* **20**, 148–156.

PIMBLEY, W. T. & LEE, H. C. 1977 Satellite droplet formation in a liquid jet. *IBM J. Res. Dev.* **21**, 21–30.

RAYLEIGH, LORD 1945 *The Theory of Sound*, vol. 2. Dover.

ROACHE, P. J. 1972 *Computational Fluid Dynamics.* Hermosa.

SCHWABE, D., SCHARMANN, A., PREISSER, F. & OEDER, R. 1978 Experiments on surface tension driven in floating zone melting. *J. Crystal Growth* **43**, 305–312.

WUEST, W. & CHUN, C. H. 1980 Oscillatory Marangoni convection. *IAF* 80-C-113, *XXXI IAF Congress, Tokyo.*